Journal of Mathematical Modeling
Vol. -, No. -, 2026, pp. -. Research Article

JMM

Fractional-order coupled dynamics of multi-region epidemics with reinfection and optimal control

Mehrab Sedighpour[†], **Mozhgan Akbari**[‡*]

[†]*Department of Applied Mathematics, Faculty of Mathematical Sciences, University of Guilan, Rasht, Iran*
[‡]*Department of Pure Mathematics, Faculty of Mathematical Sciences, University of Guilan, Rasht, Iran*

Email(s): mehrab.s5@webmail.guilan.ac.ir, m_akbari@guilan.ac.ir

Abstract. This paper proposes a coupled fractional-order SEIR model that incorporates inter-regional mobility and accounts for reinfection. By employing Caputo fractional derivatives, the framework captures non-Markovian memory effects inherent in disease transmission and progression. Analytical results establish the existence of both disease-free and endemic equilibria, with the basic reproduction number ($\mathscr{R}_0$) serving as a sharp threshold: the disease-free equilibrium is globally asymptotically stable when $\mathscr{R}_0 < 1$, whereas a unique endemic equilibrium is globally asymptotically stable when $\mathscr{R}_0 > 1$ under a specific proportionality assumption on mobility rates (see Section 5 for details), which may not hold for general empirical data. To demonstrate the model's utility in public health planning, we formulate an optimal control problem and present numerical simulations–illustrated with a representative multi-region outbreak scenario–that validate the theoretical findings and assess the impact of coordinated interventions.

Keywords: Fractional-coupled dynamical system, Caputo fractional derivatives, epidemic modeling, optimal control, stability analysis.
AMS Subject Classification 2010: 26A33, 34K37, 37M05, 34A08, 44A10.

1 Introduction

Mathematical modeling in epidemiology is an essential scientific method for understanding, predicting, and controlling the spread of diseases within populations. These models are particularly crucial during epidemics and pandemics, where they can inform public health interventions and policy-making.

*Corresponding author
Received: 04 May 2026/ Revised: 17 August 2026/ Accepted: 23 August 2026
DOI: 10.22124/jmm.2026.33451.3061

During an epidemic or pandemic, models can estimate the potential spread of the disease, evaluate intervention effectiveness, and predict healthcare system burdens. They can identify high-risk populations and inform strategies to mitigate the disease's impact. Populations are categorized into states such as Susceptible, Exposed, Infected, and Recovered (*SEIR* model), with parameters like transmission rates, recovery rates, and contact patterns used to simulate disease spread. Models can simulate scenarios, including vaccination campaigns or social distancing measures, and assist in resource distribution planning, such as vaccines or hospital beds. They can be updated with real-time data to provide current epidemic or pandemic assessments.

The application of mathematical models in epidemiology dates back to 1760 with Daniel Bernoulli's work on smallpox in England. The field advanced significantly with Ross's 1911 paper exploring malaria transmission dynamics [26]. In 1927, Kermack and McKendrick introduced the seminal *SIR* (Susceptible-Infected-Recovered) model, forming the foundation for numerous epidemic models [22]. Later models have grown in complexity, including *SEIR* (Susceptible-Exposed-Infected-Recovered), *SIS* (Susceptible-Infected-Susceptible), and network-based models, tailored to specific diseases, transmission methods, and underlying assumptions [15, 22].

Modeling, particularly disease modeling, faces challenges. Accurate modeling depends on high-quality data, which may be scarce during a rapidly evolving situation. Human behavior significantly influences disease spread, making it difficult to model these dynamics accurately. All models have inherent uncertainties, and their predictions should be interpreted with caution. In recent years, research on epidemic dynamics has increasingly emphasized the importance of community structure and human mobility in disease transmission. Lieberthal et al. (2023) illustrated that factors such as infection rates, host diffusion, and community modularity are essential in shaping the spread and control of epidemics within human metapopulation networks [19]. While multi-region compartmental configurations—such as discrete SEIRS models—have successfully integrated anthropological travel-blocking and spatial connectivity across adjacent zones [11], designing applicable spatiotemporal control systems across large geographical scales during rapidly shifting pandemic crises remains a major operational hurdle [12]. Crucially, these foundational multi-region frameworks typically rely on integer-order variations that do not fully capture the memory, hereditary traits, and non-Markovian properties of transmission dynamics, nor do they fully reconcile multi-region mobility with long-term post-recovery reinfection risks.

The model proposed in this article is designed for human-to-human transmissible epidemics, accounting for the possibility of post-recovery reinfection. This implies that individuals who have recovered may lose their immunity over time, reverting to a susceptible state. Additionally, the model allows for inter-regional population movement. Overall, this model is applicable to diseases such as tuberculosis (TB), influenza (FLU), Middle East Respiratory Syndrome (MERS), Severe Acute Respiratory Syndrome Coronavirus 2 (SARS-CoV-2), Respiratory Syncytial Virus (RSV), and other epidemics with reinfection potential.

Biological memory continuously shapes current epidemiological states through persistent immunity and evolving social behavior. To capture these history-dependent dynamics, we propose a coupled multi-region framework using Caputo fractional derivatives that accounts for both host-pathogen interactions and inter-regional mobility. By integrating population movement and memory effects, this model enhances realism and predictive power for complex multi-patch epidemics. Specifically, this study establishes the existence and uniqueness of solutions, characterizes the system's critical points, and evaluates both local and global stability to inform public health strategies. In particular, we establish the global asymptotic stability of the endemic equilibrium under sufficient algebraic conditions for a baseline sce-

nario with restricted mobility and no reinfection. Section 3 provides the fundamental mathematical analysis, including the existence of the disease-free equilibrium, the well-posedness (non-negativity and boundedness) of solutions, and the derivation of the basic reproduction number $\mathscr{R}_0$. Section 4 investigates the local and global stability of the disease-free equilibrium. Section 5 establishes the uniqueness and global asymptotic stability of the endemic equilibrium under appropriate conditions. Section 6 formulates the fractional optimal control problem and derives the necessary optimality conditions. Section 7 presents numerical simulations to validate the theoretical results and assess the impact of control measures. Finally, Section 8 concludes the paper with a summary and discussion of future work.

2 Model formulation

2.1 Model assumptions and structure

We propose a multi-region, fractional-order SEIRS epidemic model designed for diseases characterized by human-to-human transmission and waning immunity (leading to potential reinfection). This framework is applicable to a class of diseases such as influenza, tuberculosis, RSV, and coronaviruses.

The model considers n distinct regions (or patches). The population in each region is divided into four compartments:

- **Susceptible** (S_j): Individuals capable of contracting the disease.
- **Exposed** (E_j): Individuals who are infected but not yet infectious.
- **Infected** (I_j): Individuals who are infectious and can transmit the disease.
- **Recovered** (R_j): Individuals who have recovered from the disease. They lose immunity at a rate ζ_j and re-enter the susceptible compartment.

To capture spatial heterogeneity and human mobility, we incorporate population movement between these regions. We make the following key assumptions regarding mobility:

1. Individuals travel between regions while retaining their disease status (e.g., a susceptible person moves as susceptible, an infected person moves as infected).
2. The travel rates are independent of the disease dynamics and are represented by constant parameters.
3. Upon arrival in a new region, individuals immediately interact according to the local disease transmission dynamics of that region.

The disease transmission within each region j follows a bilinear incidence rate $\beta_j S_j I_j$, where β_j is the effective contact rate. The progression from exposed to infected, and from infected to recovered, occurs at rates θ_j and γ_j, respectively. Natural mortality occurs in all compartments at rate μ_j, and disease-induced mortality in the infected compartment occurs at rate δ_j. New susceptible individuals enter the population at a constant birth rate Λ_j. This bilinear form is justified by the classical mass-action principle, assuming a well-mixed population within each patch. In the multi-patch setting, migrating individuals, upon arrival, are exposed to the local transmission rate β_j and the local infection level I_j, making this formulation epidemiologically consistent under the assumptions of intra-regional homogeneity and mobility-independent contact rates (see, e.g., [16, 19]).

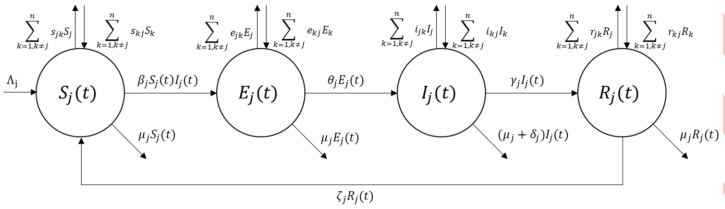

Figure 1: Schematic diagram of the model in the jth region

2.2 Mobility parameters and model equations

The movement of individuals between regions is defined by the following time-independent rates:

- s_{jk}: Movement rate from compartment S_j (region j) to compartment S_k (region k).
- e_{jk}: Movement rate from compartment E_j to compartment E_k.
- i_{jk}: Movement rate from compartment I_j to compartment I_k.
- r_{jk}: Movement rate from compartment R_j to compartment R_k.

It is necessary to note that all mobility parameters are non-negative and the natural mortality rates are strictly positive. This is a crucial biological principle, as negative mortality rates are physically impossible. Furthermore, given the distinct indices tracking inter-regional movement, travel rates between regions must naturally remain non-negative. Hence, we assume that all mobility rates are non-negative, i.e., $s_{jk}, e_{jk}, i_{jk}, r_{jk} \geq 0$ for $j \neq k$, and the natural mortality rates satisfy $\mu_j > 0$ for each j. The mobility of the infected compartment, i_{jk}, is also defined as movement from region j to region k.

Let ${}_0^cD_t^\alpha$ denote the left Caputo fractional derivative of order $\alpha \in (0,1]$, which introduces memory effects and non-Markovian dynamics into the system. The governing equations for region j are given by the following coupled fractional-order differential system:

$$\begin{cases} {}_0^cD_t^\alpha S_j &= \Lambda_j + \zeta_j R_j - \beta_j S_j I_j - \mu_j S_j + \sum_{\substack{k=1 \\ k\neq j}}^{n} (s_{kj} S_k - s_{jk} S_j), \\ {}_0^cD_t^\alpha E_j &= \beta_j S_j I_j - (\mu_j + \theta_j) E_j + \sum_{\substack{k=1 \\ k\neq j}}^{n} (e_{kj} E_k - e_{jk} E_j), \\ {}_0^cD_t^\alpha I_j &= \theta_j E_j - (\mu_j + \delta_j + \gamma_j) I_j + \sum_{\substack{k=1 \\ k\neq j}}^{n} (i_{kj} I_k - i_{jk} I_j), \\ {}_0^cD_t^\alpha R_j &= \gamma_j I_j - (\mu_j + \zeta_j) R_j + \sum_{\substack{k=1 \\ k\neq j}}^{n} (r_{kj} R_k - r_{jk} R_j), \end{cases} \tag{1}$$

subject to non-negative initial conditions $S_j(0), E_j(0), I_j(0), R_j(0) \geq 0$ for $j = 1, 2, \ldots, n$. A schematic diagram of the model dynamics for a single region j is depicted in Figure 1.

3 Analysis of the model

In this section, we establish the fundamental mathematical properties of the fractional-order multi-region system (1), including the existence and uniqueness of solutions, the existence of equilibria, the well-posedness (non-negativity and boundedness) of solutions, and the calculation of the epidemic threshold.

Theorem 1. *For any non-negative initial condition*

$$(S_j(0), E_j(0), I_j(0), R_j(0)) \in \mathbb{R}^{4n}_{\geq 0}, \qquad j = 1, \ldots, n,$$

system (1) *admits a unique global solution on* $(0, \infty)$.

Proof. System (1) can be written in the compact form

$${}_0^c D_t^\alpha X(t) = F(X(t)), \qquad X(0) = X_0,$$

where

$$X = (S_1, E_1, I_1, R_1, \ldots, S_n, E_n, I_n, R_n)^T \in \mathbb{R}^{4n},$$

and $F : \mathbb{R}^{4n} \to \mathbb{R}^{4n}$ is a locally Lipschitz continuous vector field. Indeed, the components of F are either linear or quadratic functions (due to the bilinear incidence terms $\beta_j S_j I_j$), and hence all partial derivatives are bounded on any compact subset of $\mathbb{R}^{4n}$. Therefore, by the global existence theory for fractional differential equations with Caputo derivatives [20, Theorem 2.1], there exists a unique solution for $t \geq 0$. □

3.1 Disease-free equilibrium (DFE)

At the disease-free equilibrium, the pathogen is entirely eradicated from all regions, meaning that $E_j = I_j = R_j = 0$ for all $j = 1, 2, \ldots, n$. Substituting these values into system (1) causes the infection transmission and immunity waning terms to vanish. By setting the fractional derivatives to zero, the system reduces to the following demographic balance equation for each region:

$$\Lambda_j + \sum_{\substack{k=1 \\ k \neq j}}^{n} s_{kj} S_k - \left(\mu_j + \sum_{\substack{k=1 \\ k \neq j}}^{n} s_{jk} \right) S_j = 0. \tag{2}$$

This system can be written in matrix form as:

$$\mathscr{M} S = \Lambda,$$

where

$$S = \begin{bmatrix} S_1 & S_2 & \ldots & S_n \end{bmatrix}^{\mathrm{T}}, \qquad \Lambda = \begin{bmatrix} \Lambda_1 & \Lambda_2 & \ldots & \Lambda_n \end{bmatrix}^{\mathrm{T}},$$

and $\mathscr{M}$ is an $n \times n$ matrix whose diagonal and off-diagonal entries are given by:

$$\mathscr{M}_{jj} = \mu_j + \sum_{\substack{k=1 \\ k \neq j}}^{n} s_{jk}, \qquad \mathscr{M}_{jk} = -s_{kj} \quad (j \neq k).$$

Theorem 2. *Under the given initial conditions, system* (1) *always admits a unique disease-free equilibrium* E_0.

Proof. Since all off-diagonal entries of $\mathscr{M}$ are non-positive and the sum of the entries in each column of $\mathscr{M}$ is positive, it follows from Theorem 2.3 in [4] that $\mathscr{M}$ is a nonsingular M-matrix. Hence, $\mathscr{M}^{-1} \geq 0$. Consequently, equation (2) admits a unique positive solution:

$$S^0 = \mathscr{M}^{-1}\Lambda > 0.$$

Thus, system (1) possesses a unique disease-free equilibrium of the form:

$$E_0 = \left(S_1^0, 0, 0, 0, S_2^0, 0, 0, 0, \ldots, S_n^0, 0, 0, 0\right).$$

This establishes the existence and uniqueness of E_0. □

3.2 Non-negativity and boundedness (well-posedness)

We now prove that the system is mathematically and biologically well-posed: solutions with non-negative initial data remain non-negative and are ultimately bounded for all future time.

Theorem 3. *The region*

$$\Omega^+ = \left\{(S_1, E_1, I_1, R_1, \ldots, S_n, E_n, I_n, R_n) : S_j > 0,\ E_j \geq 0,\ I_j \geq 0,\ R_j \geq 0,\ j = 1, \ldots, n\right\}$$

is a positively invariant set for system (1). Consequently, for any initial condition in Ω^+, the corresponding solution remains in Ω^+ for all $t > 0$.

Proof. We recall that the existence and uniqueness of a global solution for system (1) is guaranteed by Theorem 3.1 above. We now prove the positive invariance of Ω^+.We consider the boundary hyperplanes defined by $S_j = 0$, $E_j = 0$, $I_j = 0$, and $R_j = 0$, respectively. It is straightforward to verify that the right-hand side of system (1) is quasi-positive, since each equation contains only nonnegative cross-interaction terms. On the hyperplanes of region Ω^+, we have

$$\begin{aligned}
{}_0^c D_t^\alpha S_j\big|_{S_j=0} &= \Lambda_j + \zeta_j R_j + \sum_{k\neq j} s_{kj} S_k \geq \Lambda_j > 0,\\
{}_0^c D_t^\alpha E_j\big|_{E_j=0} &= \beta_j S_j I_j + \sum_{k\neq j} e_{kj} E_k \geq 0,\\
{}_0^c D_t^\alpha I_j\big|_{I_j=0} &= \theta_j E_j + \sum_{k\neq j} i_{kj} I_k \geq 0,\\
{}_0^c D_t^\alpha R_j\big|_{R_j=0} &= \gamma_j I_j + \sum_{k\neq j} r_{kj} R_k \geq 0.
\end{aligned}$$

Therefore, by the standard invariance theorem for Caputo fractional differential systems (see Theorem 3.1 in [2]), the region Ω^+ is positively invariant. Hence, any solution starting from Ω^+ remains in Ω^+ for all $t > 0$. □

Before establishing the qualitative properties of system (1), we show that its solutions remain bounded for all $t \geq 0$ and eventually enter a compact positively invariant region. Let

$$N(t) = \sum_{j=1}^{n} \left(S_j(t) + E_j(t) + I_j(t) + R_j(t)\right)$$

denote the total population of all regions, and define

$$\bar{\Lambda} = \sum_{j=1}^{n} \Lambda_j, \qquad \mu = \min_{1\le j\le n}\{\mu_j\} > 0.$$

The following theorem provides a positively invariant attracting set for system (1).

Theorem 4. *System (1) with initial conditions in $\mathbb{R}^{4n}_{\ge 0}$ is uniformly bounded. Moreover, the set*

$$\Omega = \left\{ (S_1, E_1, I_1, R_1, \ldots, S_n, E_n, I_n, R_n) \in \Omega^+ : \sum_{j=1}^{n} (S_j + E_j + I_j + R_j) \le \frac{\bar{\Lambda}}{\mu} \right\}$$

is positively invariant and attracting. In particular,

$$\limsup_{t\to\infty} N(t) \le \frac{\bar{\Lambda}}{\mu}.$$

Proof. Let

$$N(t) = \sum_{j=1}^{n} (S_j(t) + E_j(t) + I_j(t) + R_j(t))$$

be the total population. Summing all equations of system (1) for $j = 1, \ldots, n$ gives

$${}_0^c D_t^{\alpha} N(t) = \sum_{j=1}^{n} \Lambda_j - \sum_{j=1}^{n} \mu_j (S_j + E_j + I_j + R_j) - \sum_{j=1}^{n} \delta_j I_j.$$

Since

$$\mu_j \ge \mu = \min_{1\le j\le n}\{\mu_j\} > 0, \qquad \delta_j I_j \ge 0,$$

it follows that

$${}_0^c D_t^{\alpha} N(t) \le \bar{\Lambda} - \mu N(t), \tag{3}$$

where

$$\bar{\Lambda} = \sum_{j=1}^{n} \Lambda_j.$$

Consider the auxiliary problem

$${}_0^c D_t^{\alpha} \widetilde{N}(t) = \bar{\Lambda} - \mu \widetilde{N}(t), \qquad \widetilde{N}(0) = N(0).$$

By the comparison principle for systems of Caputo fractional differential equations [29], and the fact that the right-hand side is monotone increasing in $N(t)$, we obtain

$$N(t) \le \widetilde{N}(t), \qquad t \ge 0.$$

The explicit solution is

$$\widetilde{N}(t) = \widetilde{N}(0) E_{\alpha,1}(-\mu t^{\alpha}) + \bar{\Lambda} t^{\alpha} E_{\alpha,\alpha+1}(-\mu t^{\alpha}),$$

where $E_{\alpha,\beta}$ denotes the Mittag-Leffler function [23]. Using

$$\lim_{t\to\infty} E_{\alpha,1}(-\mu t^{\alpha}) = 0, \qquad \lim_{t\to\infty} t^{\alpha} E_{\alpha,\alpha+1}(-\mu t^{\alpha}) = \frac{1}{\mu},$$

we obtain

$$\limsup_{t\to\infty} \widetilde{N}(t) = \frac{\bar{\Lambda}}{\mu}.$$

Hence,

$$\limsup_{t\to\infty} N(t) \leq \frac{\bar{\Lambda}}{\mu},$$

which proves the ultimate boundedness of the total population.

Next, we verify the positive invariance of Ω. Suppose that

$$\sum_{j=1}^{n} (S_j + E_j + I_j + R_j) = \frac{\bar{\Lambda}}{\mu}.$$

Then, by inequality (3),

$${}_0^c D_t^{\alpha} N(t) \leq \bar{\Lambda} - \mu \frac{\bar{\Lambda}}{\mu} = 0.$$

Therefore, the Caputo derivative is nonpositive on the boundary of Ω, implying that trajectories cannot cross the boundary outward. Consequently, every solution starting in Ω remains in Ω for all $t \geq 0$, and Ω is positively invariant.

Finally, since all state variables are nonnegative and satisfy

$$S_j(t), E_j(t), I_j(t), R_j(t) \leq N(t), \qquad j = 1, \ldots, n,$$

every component of the solution is bounded by the total population. Therefore, all solutions are uniformly bounded and eventually enter the compact attracting set Ω. □

Corollary 1. *The biologically feasible region Ω defined in Theorem 4 is a compact, positively invariant, and globally attracting set for system (1). All subsequent analysis can be restricted to Ω.*

3.3 Basic reproduction number

To derive the basic reproduction number, we focus solely on the compartments involved in the transmission process. Thus, we define

$$u = \begin{bmatrix} E_1 & E_2 & \cdots & E_n & I_1 & I_2 & \cdots & I_n \end{bmatrix}^{\top}.$$

The right-hand sides of the second and third equations of system (1) can be expressed as $\mathscr{F} - \mathscr{V}$, where

$$\mathscr{F} = \begin{bmatrix} \beta_1 I_1 S_1 \\ \beta_2 I_2 S_2 \\ \vdots \\ \beta_n I_n S_n \\ 0 \\ 0 \\ \vdots \\ 0 \end{bmatrix}, \qquad \mathscr{V} = \begin{bmatrix} -\sum_{k=2}^{n} e_{k1} E_k + \left(\mu_1 + \theta_1 + \sum_{k=2}^{n} e_{1k}\right) E_1 \\ -\sum_{\substack{k=1 \\ k\neq 2}}^{n} e_{k2} E_k + \left(\mu_2 + \theta_2 + \sum_{\substack{k=1 \\ k\neq 2}}^{n} e_{2k}\right) E_2 \\ \vdots \\ -\sum_{k=1}^{n-1} e_{kn} E_k + \left(\mu_n + \theta_n + \sum_{k=1}^{n-1} e_{nk}\right) E_n \\ -\theta_1 E_1 - \sum_{k=2}^{n} i_{k1} I_k + \left(\mu_1 + \delta_1 + \gamma_1 + \sum_{k=2}^{n} i_{1k}\right) I_1 \\ -\theta_2 E_2 - \sum_{\substack{k=1 \\ k\neq 2}}^{n} i_{k2} I_k + \left(\mu_2 + \delta_2 + \gamma_2 + \sum_{\substack{k=1 \\ k\neq 2}}^{n} i_{2k}\right) I_2 \\ \vdots \\ -\theta_n E_n - \sum_{k=1}^{n-1} i_{kn} I_k + \left(\mu_n + \delta_n + \gamma_n + \sum_{k=1}^{n-1} i_{nk}\right) I_n \end{bmatrix}.$$

The Jacobian matrices at the disease-free equilibrium are then given by

$$F = \begin{bmatrix} 0 & F_{12} \\ 0 & 0 \end{bmatrix}_{2n\times 2n}, \qquad V = \begin{bmatrix} V_{11} & 0 \\ V_{21} & V_{22} \end{bmatrix}_{2n\times 2n},$$

where

$$F_{12} = \begin{bmatrix} \beta_1 S_1^0 & \cdots & 0 \\ \vdots & \ddots & \vdots \\ 0 & \cdots & \beta_n S_n^0 \end{bmatrix}, V_{11} = \begin{bmatrix} \mu_1 + \theta_1 + \sum_{k=2}^{n} e_{1k} & \cdots & -e_{n1} \\ -e_{12} & \cdots & -e_{n2} \\ \vdots & \ddots & \vdots \\ -e_{1n} & \cdots & \mu_n + \theta_n + \sum_{k=1}^{n-1} e_{nk} \end{bmatrix},$$

$$V_{21} = \begin{bmatrix} -\theta_1 & \cdots & 0 \\ \vdots & \ddots & \vdots \\ 0 & \cdots & -\theta_n \end{bmatrix}, V_{22} = \begin{bmatrix} \mu_1 + \delta_1 + \gamma_1 + \sum_{k=2}^{n} i_{1k} & \cdots & -i_{n1} \\ \vdots & \ddots & \vdots \\ -i_{1n} & \cdots & \mu_n + \delta_n + \gamma_n + \sum_{k=1}^{n-1} i_{nk} \end{bmatrix}.$$

Since V is a nonsingular M-matrix and $V^{-1} \geq 0$ [4], the next-generation matrix FV^{-1} is nonnegative. Following the method of van den Driessche and Watmough [27], we have

$$\mathscr{R}_0 = \rho(FV^{-1}) = \rho\left(F_{12} V_{21} V_{11}^{-1} V_{22}^{-1}\right).$$

where $\rho(\cdot)$ denotes the spectral radius of a matrix. In the decoupled (no-mobility) case, where each patch is isolated from the others, the basic reproduction number of patch j is given by [27], In this case, the disease-free equilibrium reduces to $S_j^0 = \Lambda_j/\mu_j$, yielding

$$\mathscr{R}_0^{(j)} = \frac{\beta_j \theta_j \Lambda_j}{\mu_j(\mu_j + \theta_j)(\mu_j + \gamma_j + \delta_j)}.$$

In contrast, in the presence of inter-regional mobility, the disease-free equilibrium is no longer decoupled and is given by

$$S^0 = \mathscr{M}^{-1}\Lambda,$$

where $\mathscr{M}$ is the mobility-adjusted demographic matrix. In this case, $\mathscr{R}_0 = \rho(FV^{-1})$ serves as the global threshold parameter for the stability of the disease-free equilibrium.

Thus, $\mathscr{R}_0$ is the spectral radius of the next-generation matrix, which serves as the threshold parameter for the stability of the disease-free equilibrium.

4 Stability of the disease-free equilibrium

In this section, we investigate the local and global stability of the disease-free equilibrium E_0 and demonstrate that no equilibrium other than E_0 exists on the boundary of Ω.

Theorem 5. *If $\mathscr{R}_0 < 1$, then E_0 is locally asymptotically stable. If $\mathscr{R}_0 > 1$, then E_0 is unstable.*

Proof. We order the variables as $E_1,\dots,E_n,I_1,\dots,I_n,S_1,\dots,S_n,R_1,\dots,R_n$. The jacobian matrix of system (1) at the disease-free equilibrium is given by

$$\mathscr{J}_{E_0} = \begin{bmatrix} F-V & 0 & 0 \\ \begin{bmatrix} 0 & -F_{12} \end{bmatrix} & -\mathscr{M} & D \\ \begin{bmatrix} 0 & B \end{bmatrix} & 0 & -C \end{bmatrix},$$

where

$$B = \begin{bmatrix} \gamma_1 & & \\ & \ddots & \\ & & \gamma_n \end{bmatrix}, \qquad C = \begin{bmatrix} \mu_1+\zeta_1+\sum_{k=2}^{n} r_{1k} & \cdots & -r_{n1} \\ \vdots & \ddots & \vdots \\ -r_{1n} & \cdots & \mu_n+\zeta_n+\sum_{k=1}^{n-1} r_{nk} \end{bmatrix},$$

$$D = \begin{bmatrix} \zeta_1 & & \\ & \ddots & \\ & & \zeta_n \end{bmatrix}.$$

Since $\mathscr{M}$ and C are nonsingular M-matrices [4], all eigenvalues of $-\mathscr{M}$ and $-C$ satisfy $\Re(\lambda) < 0$. Moreover, from [8, 27], we have

$$\rho(FV^{-1}) < 1 \quad \Leftrightarrow \quad \sigma(F-V) < 0,$$

where $\sigma(F-V)$ denotes the spectral abscissa of $F-V$. This implies that all eigenvalues of $F-V$ satisfy $\Re(\lambda) < 0$.

For fractional-order systems with $0 < \alpha < 1$, the equilibrium is asymptotically stable if all eigenvalues λ satisfy

$$|\arg(\lambda)| > \frac{\alpha\pi}{2},$$

which is guaranteed when $\Re(\lambda) < 0$ since $|\arg(\lambda)| > \frac{\pi}{2} > \frac{\alpha\pi}{2}$.

Hence, if $\mathscr{R}_0 = \rho(FV^{-1}) < 1$, all eigenvalues of $\mathscr{J}_{E_0}$ lie in the stability region and the DFE is locally asymptotically stable.

If $\mathscr{R}_0 > 1$, then $F-V$ has at least one eigenvalue with $\Re(\lambda) > 0$, and therefore the equilibrium becomes unstable. Thus, the disease-free equilibrium is locally asymptotically stable if $\mathscr{R}_0 < 1$ and unstable if $\mathscr{R}_0 > 1$. □

Theorem 6. *Suppose that $\mathscr{M}_E = (e_{kj})$ and $\mathscr{M}_I = (i_{kj})$ are irreducible, meaning that the graph of the patches is strongly connected through the movement of exposed and infected individuals. Then no equilibrium other than E_0 exists on the boundary of Ω.*

Remark 1. *Mathematically, the irreducibility of the movement matrices $\mathscr{M}_E = (e_{kj})$ and $\mathscr{M}_I = (i_{kj})$ means that their corresponding directed mobility graphs are strongly connected [6]. Epidemiologically, this assumption implies that there exists at least one sequence of positive mobility rates connecting any patch j to any other patch k, either directly or through intermediate patches.In human metapopulation networks (such as interconnected cities, commuting corridors, or regional transportation grids), complete connectivity is standard over extended time horizons, as human movement typically forms a unified network [24]. For empirical applications, irreducibility can be readily verified from origin-destination mobility matrices obtained from cell phone location data, census transport surveys, or flight networks.*

Proof of Theorem 6. We show that if $E_j = 0$ or $I_j = 0$ for some j, then $E_k = I_k = 0$ for all k. If $I_j = 0$, from the third equation of system (1) we obtain

$$\theta_j E_j + \sum_{\substack{k=1 \\ k\neq j}}^{n} i_{kj} I_k = 0.$$

Since $\theta_j > 0$, it follows that $E_j = 0$ and $I_k = 0$ whenever $i_{kj} > 0$. From the second equation of system (1), we have

$$\sum_{\substack{k=1 \\ k\neq j}}^{n} e_{kj} E_k = 0.$$

Thus, for all j,k with $i_{kj} > 0$ and $e_{kj} > 0$, we obtain $I_k = E_k = 0$. By the irreducibility assumptions, there exist sequences of ordered pairs connecting any patch j to any patch k via positive entries of $\mathscr{M}_E$ and $\mathscr{M}_I$. Consequently, $I_k = E_k = 0$ for every k. By Theorem 2, the only equilibrium on the boundary of Ω is E_0. □

Theorem 7. *Suppose that $\mathscr{M}_E = (e_{kj})$ and $\mathscr{M}_I = (i_{kj})$ are irreducible. If $\mathscr{R}_0 < 1$, then E_0 is globally asymptotically stable in Ω. If $\mathscr{R}_0 > 1$, then E_0 is unstable, system (1) is uniformly persistent, and there exists an endemic equilibrium E^* in the interior of Ω.*

Proof. Consider a solution $(S_1, E_1, I_1, R_1, \ldots, S_n, E_n, I_n, R_n)$ to system (1) starting from initial conditions within Ω. By Theorem 4.2, E_0 is the only equilibrium on the boundary of Ω.

Since $S_j \leq S_j^0$, we obtain

$${}_0^c D_t^\alpha E_j \leq \beta_j S_j^0 I_j + \sum_{\substack{k=1 \\ k\neq j}}^{n} e_{kj} E_k - \left(\mu_j + \theta_j + \sum_{\substack{k=1 \\ k\neq j}}^{n} e_{jk} \right) E_j.$$

We consider the following linear comparison system:

$$\begin{cases} {}_0^c D_t^\alpha E_j = \beta_j S_j^0 I_j + \sum_{\substack{k=1 \\ k\neq j}}^{n} e_{kj} E_k - \left(\mu_j + \theta_j + \sum_{\substack{k=1 \\ k\neq j}}^{n} e_{jk} \right) E_j, \\ {}_0^c D_t^\alpha I_j = \theta_j E_j + \sum_{\substack{k=1 \\ k\neq j}}^{n} i_{kj} I_k - \left(\mu_j + \delta_j + \gamma_j + \sum_{\substack{k=1 \\ k\neq j}}^{n} i_{jk} \right) I_j, \end{cases} \tag{4}$$

whose coefficient matrix is precisely $F - V$.

To justify the application of the comparison principle, we note that the vector field in (4) is quasi-monotone non-decreasing. Indeed, the matrix $F-V$ is quasi-monotone since all off-diagonal entries are non-negative:

- The coupling term from E_k to E_j is $e_{kj} \geq 0$;
- The coupling term from E_j to I_j is $\theta_j \geq 0$;
- The coupling term from I_k to I_j is $i_{kj} \geq 0$.

Therefore, by the comparison principle for Caputo fractional systems [2,29], the solutions of the original system are bounded above by those of the linear comparison system (4).

For $\mathscr{R}_0 < 1$, we have $\sigma(F-V) < 0$, so all eigenvalues of $F-V$ have negative real parts, which implies Mittag–Leffler stability of the linear Caputo system [23]. Hence $E_j(t) \to 0$ and $I_j(t) \to 0$ as $t \to \infty$.

From the fourth equation, $R_j(t) \to 0$, and substituting into the first equation yields

$$ {}_0^cD_t^{\alpha} S(t) = \Lambda - \mathscr{M} S(t). $$

Using the Mittag–Leffler representation, $S(t) = S^0 + E_{\alpha,1}(-\mathscr{M} t^{\alpha})(S(0) - S^0)$, and since $-\mathscr{M}$ has all eigenvalues with negative real parts, we obtain $S(t) \to S^0$ as $t \to \infty$.

Therefore, E_0 is globally asymptotically stable when $\mathscr{R}_0 < 1$.

If $\mathscr{R}_0 > 1$, Theorem 4.1 implies instability of E_0. Using a standard uniform persistence theorem [18] and arguments in [16], and noting that the system is dissipative (Theorem 3.4), positively invariant (Theorem 3.3), and the infection subsystem is irreducible, we conclude uniform persistence of system (1). Consequently, there exists at least one endemic equilibrium E^* in the interior of Ω (see [5, 25, 30]). □

5 Uniqueness and global stability of the endemic equilibrium (EE)

Having analyzed the stability of the disease-free equilibrium, we now investigate the endemic equilibrium E^*, which represents a state where the disease persists in the population. In this section, we establish the conditions under which E^* is unique and globally asymptotically stable. To this end, we first recall a key property of the fractional derivative (see Lemma 1 below), which serves as the basis for constructing the Lyapunov function. Subsequently, we construct a suitable Lyapunov function and apply graph-theoretic techniques [9, 17] together with the fractional LaSalle invariance principle [14].

Lemma 1. *Let $x(t) \in \mathbb{R}_+$ be a continuous and differentiable function, and let $x^* \in \mathbb{R}_+$ be a constant. Then, for any $t \geq 0$ and $0 < \alpha < 1$,*

$$ {}_0^cD_t^{\alpha} \left(x(t) - x^* - x^* \ln \frac{x(t)}{x^*} \right) \leq \left(1 - \frac{x^*}{x(t)} \right) {}_0^cD_t^{\alpha} x(t). $$

For $\alpha = 1$, the inequality becomes an equality.

Proof. See Lemma 3.1 in [28]. □

Theorem 8. *Assume that $\mathscr{M}_E = (e_{kj})$ and $\mathscr{M}_I = (i_{kj})$ are irreducible. As a special case of system (1), consider the scenario where $s_{kj} = r_{kj} = 0$, and $\zeta_j = 0$ for all $j,k = 1,\dots,n$. If $\mathscr{R}_0 > 1$ and $E^* = (S_1^*, E_1^*, I_1^*, \dots, S_n^*, E_n^*, I_n^*)$ is an endemic equilibrium of system (6), then under the following sufficient algebraic condition*

$$\frac{\beta_j I_j^* S_j^*}{\theta_j E_j^*} i_{kj} I_k^* = \lambda\, e_{kj} E_k^*, \tag{5}$$

for all $j,k = 1,\dots,n$ and some $\lambda > 0$, E^* is unique and globally asymptotically stable in the interior of Ω.

Proof. When $\zeta_j = 0$ for all $j = 1,\dots,n$, system (1) reduces to the subsystem (6). Since R_j does not appear in the first three equations, it is decoupled from the other equations. Therefore, it suffices to study the stability of the following reduced subsystem:

$$\begin{cases} {}_0^cD_t^\alpha S_j = \Lambda_j - \beta_j I_j S_j - \mu_j S_j + \sum_{\substack{k=1\\k\neq j}}^n \left(s_{kj} S_k - s_{jk} S_j\right), \\ {}_0^cD_t^\alpha E_j = \beta_j I_j S_j - (\mu_j + \theta_j) E_j + \sum_{\substack{k=1\\k\neq j}}^n \left(e_{kj} E_k - e_{jk} E_j\right), \\ {}_0^cD_t^\alpha I_j = \theta_j E_j - (\mu_j + \delta_j + \gamma_j) I_j + \sum_{\substack{k=1\\k\neq j}}^n \left(i_{kj} I_k - i_{jk} I_j\right). \end{cases} \tag{6}$$

The reduced subsystem (6) has the endemic equilibrium $E^* = (S_1^*, E_1^*, I_1^*, \dots, S_n^*, E_n^*, I_n^*)$. To analyze its global stability, we construct the following Lyapunov function:

For each $j = 1,\dots,n$, define

$$V_j = \left(S_j - S_j^* - S_j^* \ln \frac{S_j}{S_j^*}\right) + \left(E_j - E_j^* - E_j^* \ln \frac{E_j}{E_j^*}\right) + \frac{\beta_j S_j^* I_j^*}{\theta_j E_j^*} \left(I_j - I_j^* - I_j^* \ln \frac{I_j}{I_j^*}\right).$$

Each V_j is nonnegative and vanishes only at E^*. By Lemma 5.1, we have

$${}_0^cD_t^\alpha V_j(t) \le \left(1 - \frac{S_j^*}{S_j}\right) {}_0^cD_t^\alpha S_j(t) + \left(1 - \frac{E_j^*}{E_j}\right) {}_0^cD_t^\alpha E_j(t) + \frac{\beta_j S_j^* I_j^*}{\theta_j E_j^*} \left(1 - \frac{I_j^*}{I_j}\right) {}_0^cD_t^\alpha I_j(t).$$

Substituting system (6) and using the equilibrium relations, we obtain

$$\begin{aligned} {}_0^cD_t^\alpha V_j(t) \le\ & \beta_j I_j^* S_j^* \left(3 - \frac{S_j^*}{S_j} - \frac{S_j E_j^* I_j}{S_j^* E_j I_j^*} - \frac{E_j I_j^*}{E_j^* I_j}\right) \\ & + \mu_j S_j^* \left(2 - \frac{S_j}{S_j^*} - \frac{S_j^*}{S_j}\right) \\ & + \sum_{\substack{k=1\\k\neq j}}^n e_{kj} E_k^* \left(1 + \frac{E_k}{E_k^*} - \frac{E_j}{E_j^*} - \frac{E_j^* E_k}{E_j E_k^*}\right) \\ & + \sum_{\substack{k=1\\k\neq j}}^n \frac{\beta_j S_j^* I_j^*}{\theta_j E_j^*} i_{kj} I_k^* \left(1 + \frac{I_k}{I_k^*} - \frac{I_j}{I_j^*} - \frac{I_j^* I_k}{I_j I_k^*}\right). \end{aligned}$$

Using the inequality $1-x+\ln x \le 0$ for $x>0$, with equality if and only if $x=1$, we obtain

$$ {}_0^cD_t^\alpha V_j(t) \le \sum_{\substack{k=1\\k\neq j}}^{n} e_{kj}E_k^* \left[\mathscr{G}_k(E_k,I_k)-\mathscr{G}_j(E_j,I_j)\right], $$

where

$$ \mathscr{G}_j(E_j,I_j) = \frac{E_j}{E_j^*} - \ln\frac{E_j}{E_j^*} + \lambda\left(\frac{I_j}{I_j^*} - \ln\frac{I_j}{I_j^*}\right), $$

and $\lambda>0$ is the constant from the compatibility condition.

Now consider a weight matrix $W=[w_{kj}]$ with entries $w_{jk}=e_{kj}E_k^*$, and let (G,W) denote the corresponding weighted directed graph. For each vertex j, define

$$ c_j = \sum_{T\in\mathscr{T}_j} w(T) \ge 0, $$

where $\mathscr{T}_j$ is the set of all spanning trees of (G,W) rooted at j, and $w(T)$ denotes the product of the weights of all arcs in T. By the matrix-tree theorem (see [17]), we have

$$ \sum_{j=1}^{n} c_j \sum_{\substack{k=1\\k\neq j}}^{n} e_{kj}E_k^* \left[\mathscr{G}_k(E_k,I_k)-\mathscr{G}_j(E_j,I_j)\right] = 0. $$

Define

$$ V(t) = \sum_{j=1}^{n} c_j V_j(t). $$

Then

$$ {}_0^cD_t^\alpha V(t) = \sum_{j=1}^{n} c_j\, {}_0^cD_t^\alpha V_j(t) \le 0 $$

for all points in the interior of Ω. Hence, by Theorem 3.1 in [17], V is a Lyapunov function for system (6).

Since $\mathscr{M}_E$ and $\mathscr{M}_I$ are irreducible, from Theorem 2.1 in [17], we have $c_j>0$ for all j.

Let

$$ \mathscr{N} = \left\{(S,E,I)\in\Omega : {}_0^cD_t^\alpha V(t)=0\right\}. $$

From the equality conditions $1-x+\ln x=0$, which hold if and only if $x=1$, we obtain

$$ \frac{S_j^*}{S_j}=1, \qquad \frac{S_jE_j^*I_j}{S_j^*E_jI_j^*}=1, \qquad \frac{E_jI_j^*}{E_j^*I_j}=1. $$

These imply

$$ S_j=S_j^*, \qquad E_j=\frac{E_j^*}{I_j^*}I_j. $$

Substituting into the first equation of system (6) at equilibrium, we get

$$ 0 = {}_0^cD_t^\alpha S_j^* = \beta_j S_j^*I_j^*\left(1-\frac{I_j}{I_j^*}\right), $$

which yields $I_j = I_j^*$ and consequently $E_j = E_j^*$ for all j. Therefore the largest invariant subset contained in $\{{}_0^cD_t^\alpha V = 0\}$ consists only of the endemic equilibrium. By the fractional LaSalle invariance principle [14], every solution starting in the interior of Ω converges to E^*. Consequently, E^* is globally asymptotically stable in the interior of Ω. Finally, uniqueness follows immediately since every endemic equilibrium must belong to the largest invariant set, which consists only of E^*. □

Remark 2. *Condition (5) is a sufficient algebraic condition that facilitates the cancellation of cross-patch flux terms in the Caputo derivative of the global Lyapunov function. While mathematically restrictive — as it considers a special case where mobility in certain compartments is constrained ($s_{kj} = r_{kj} = 0$) and reinfection is absent ($\zeta_j = 0$) — it provides an analytical baseline for stability in coupled networks.*

6 Fractional optimal control of the model

In this section, we incorporate time-dependent controls into system (1) aimed at controlling the spread of the disease. Let $u_j(t)$ be a preventive control, such as health orders and vaccinations, in region j in order to reduce transmission of infection to susceptible individuals. In $(1-u_j(t))\beta_j$, the factor $(1-u_j(t))$ denotes the reduction in β_j, the transmission rate of infection to susceptible individuals in region j, generated by the control $u_j(t)$.

The controlled system is given by

$$\begin{cases} {}_0^cD_t^\alpha S_j &= \Lambda_j + \zeta_j R_j - \beta_j(1-u_j) I_j S_j - \mu_j S_j + \sum_{\substack{k=1 \\ k\neq j}}^n \left(s_{kj}S_k - s_{jk}S_j\right), \\ {}_0^cD_t^\alpha E_j &= \beta_j(1-u_j) I_j S_j - (\mu_j + \theta_j) E_j + \sum_{\substack{k=1 \\ k\neq j}}^n \left(e_{kj}E_k - e_{jk}E_j\right), \\ {}_0^cD_t^\alpha I_j &= \theta_j E_j - (\mu_j + \delta_j + \gamma_j) I_j + \sum_{\substack{k=1 \\ k\neq j}}^n \left(i_{kj}I_k - i_{jk}I_j\right), \\ {}_0^cD_t^\alpha R_j &= \gamma_j I_j - \mu_j R_j + \sum_{\substack{k=1 \\ k\neq j}}^n \left(r_{kj}R_k - r_{jk}R_j\right). \end{cases} \tag{7}$$

We investigate the optimal level of control efforts to minimize the number of infected individuals in all regions and the cost of applying the control $u_j(t)$. This is done by minimizing the following objective functional:

$$J(u) = \int_0^{t_f} \sum_{j=1}^n \left[A_j I_j(t) + \frac{1}{2} B_j u_j^2(t)\right] dt, \tag{8}$$

where A_j and B_j are positive weight constants for $j = 1, \ldots, n$. This objective functional balances the dual priorities of controlling the disease outbreak and managing the socio-economic expenditure of the intervention. The linear components $A_j I_j(t)$ represent the public health priority to minimize active infections across all regions, while the control variables $u_j(t)$ enter the functional quadratically to model a convex cost structure. This captures the increasing marginal difficulty and expense associated with intensive public health campaigns, and guarantees the strict convexity of the Hamiltonian $\mathscr{H}$ with respect to the controls, ensuring a well-defined, continuous optimal control solution.

6.1 Existence of an optimal control

The existence of an optimal control u^* for the fractional optimal control problem (7)-(8) follows from the Filippov-Cesari theorem [7, 13]. Since the control set $U = [0, u_{\max}]^n$ is convex and compact, the state

dynamics are linear in the control variables, and the integrand of the cost functional is convex in u, the standard existence theorem for fractional optimal control problems applies (see, e.g., [3,21]).

6.2 Fractional pontryagin maximum principle

The Hamiltonian for the optimal control problem is defined using the right-hand side functions of the state equations:

$$\begin{aligned}\mathscr{H} = \sum_{j=1}^{n} \Bigg[& A_j I_j + \frac{1}{2} B_j u_j^2 + \lambda_j^1 \left(\Lambda_j + \zeta_j R_j - \beta_j (1-u_j) I_j S_j - \mu_j S_j + \sum_{\substack{k=1 \\ k\neq j}}^{n} \left(s_{kj} S_k - s_{jk} S_j \right) \right) \\ & + \lambda_j^2 \left(\beta_j (1-u_j) I_j S_j - (\mu_j + \theta_j) E_j + \sum_{\substack{k=1 \\ k\neq j}}^{n} \left(e_{kj} E_k - e_{jk} E_j \right) \right) \\ & + \lambda_j^3 \left(\theta_j E_j - (\mu_j + \delta_j + \gamma_j) I_j + \sum_{\substack{k=1 \\ k\neq j}}^{n} \left(i_{kj} I_k - i_{jk} I_j \right) \right) \\ & + \lambda_j^4 \left(\gamma_j I_j - \mu_j R_j + \sum_{\substack{k=1 \\ k\neq j}}^{n} \left(r_{kj} R_k - r_{jk} R_j \right) \right) \Bigg].\end{aligned} \tag{9}$$

Using the necessary conditions for fractional optimal control problems (see [1,3,21]), the adjoint variables satisfy the right-sided Caputo fractional differential equations:

$${}_t^c D_{t_f}^{\alpha} \lambda_j^1(t) = \frac{\partial \mathscr{H}}{\partial S_j}(t), \tag{10}$$

$${}_t^c D_{t_f}^{\alpha} \lambda_j^2(t) = \frac{\partial \mathscr{H}}{\partial E_j}(t), \tag{11}$$

$${}_t^c D_{t_f}^{\alpha} \lambda_j^3(t) = \frac{\partial \mathscr{H}}{\partial I_j}(t), \tag{12}$$

$${}_t^c D_{t_f}^{\alpha} \lambda_j^4(t) = \frac{\partial \mathscr{H}}{\partial R_j}(t), \tag{13}$$

with terminal conditions $\lambda_j^1(t_f) = \lambda_j^2(t_f) = \lambda_j^3(t_f) = \lambda_j^4(t_f) = 0$, where ${}_t^c D_{t_f}^{\alpha}$ denotes the right-sided Caputo fractional derivative of order α.
Explicitly, the adjoint equations are

$$\begin{cases} {}_t^c D_{t_f}^{\alpha} \lambda_j^1(t) & = \beta_j I_j (1-u_j)(\lambda_j^2 - \lambda_j^1) - \mu_j \lambda_j^1 + \sum_{\substack{k=1 \\ k\neq j}}^{n} s_{jk} (\lambda_k^1 - \lambda_j^1), \\ {}_t^c D_{t_f}^{\alpha} \lambda_j^2(t) & = \theta_j (\lambda_j^3 - \lambda_j^2) - \mu_j \lambda_j^2 + \sum_{\substack{k=1 \\ k\neq j}}^{n} e_{jk} (\lambda_k^2 - \lambda_j^2), \\ {}_t^c D_{t_f}^{\alpha} \lambda_j^3(t) & = A_j + \beta_j S_j (1-u_j)(\lambda_j^2 - \lambda_j^1) + \gamma_j (\lambda_j^4 - \lambda_j^3) - (\mu_j + \delta_j) \lambda_j^3 \\ & \quad + \sum_{\substack{k=1 \\ k\neq j}}^{n} i_{jk} (\lambda_k^3 - \lambda_j^3), \\ {}_t^c D_{t_f}^{\alpha} \lambda_j^4(t) & = \zeta_j (\lambda_j^1 - \lambda_j^4) - \mu_j \lambda_j^4 + \sum_{\substack{k=1 \\ k\neq j}}^{n} r_{jk} (\lambda_k^4 - \lambda_j^4). \end{cases} \tag{14}$$

The terminal conditions are

$$S_j(0) = S_j^0, \quad E_j(0) = E_j^0, \quad I_j(0) = I_j^0, \quad R_j(0) = R_j^0,$$
$$\lambda_j^1(t_f) = 0, \quad \lambda_j^2(t_f) = 0, \quad \lambda_j^3(t_f) = 0, \quad \lambda_j^4(t_f) = 0, \qquad j = 1, \ldots, n.$$

The optimal controls u_j^* are characterized by the stationarity condition $\frac{\partial \mathscr{H}}{\partial u_j} = 0$, which yields

$$\frac{\partial \mathscr{H}}{\partial u_j} = B_j u_j - \beta_j I_j S_j (\lambda_j^2 - \lambda_j^1) = 0.$$

Taking into account the control bounds $0 \leq u_j(t) \leq u_{j,\max}$, we obtain

$$u_j^*(t) = \min\left(u_{j,\max}, \max\left(0, \frac{\beta_j I_j S_j (\lambda_j^2 - \lambda_j^1)}{B_j}\right)\right), \qquad j = 1, \ldots, n. \tag{15}$$

Since $B_j > 0$, the Hamiltonian is strictly convex with respect to u_j. Therefore, the stationary condition admits a unique minimizer, which is given by the optimal control characterization (15). The optimal control problem consists of solving the state system (7) forward in time with initial conditions, the adjoint system (10)-(13) backward in time with terminal conditions, together with the optimal control characterization (15).

7 Numerical experiments

In this paper, a hybrid numerical framework is proposed to simulate the fractional-order system dynamics and solve the corresponding optimal control problem. For the forward-in-time state simulations across various fractional orders α, the fractional Adams-Bashforth-Moulton predictor-corrector (PECE) scheme is utilized, which robustly captures the non-local memory effects and ensures high numerical stability [10]. Furthermore, to solve the bounded fractional optimal control problem, this integration scheme is embedded within the Forward-Backward Sweep Method (FBSM) based on Pontryagin's Maximum Principle [3]. Within this iterative process, the state equations are integrated forward in time, while the co-state (adjoint) equations are solved backward in time using a time-reversed variable $\tau = T - t$. The control variables are iteratively updated and clipped to satisfy constraints until the system converges below a prescribed tolerance (tol $= 10^{-4}$).

In this section, we perform comprehensive numerical simulations of the proposed fractional-order coupled SEIRS system under the Caputo derivative to evaluate its dynamic behavior, validate theoretical thresholds, and assess optimal control efficiency. Importantly, while theoretical global stability proof in Section 5 is established for a baseline special case, the numerical experiments here encompass the full multi-region framework with active reinfection ($\zeta_j > 0$) and inter-patch mobility across all compartments. Rather than performing an empirical parameter-fitting or forecasting study, we construct a representative benchmark scenario parameterized using empirical baseline ranges from the COVID-19 outbreaks in Arizona (Patch 1) and Utah (Patch 2) recorded in August 2020. All rate parameters are expressed in units of day^{-1}.

To incorporate realistic epidemiological characteristics while addressing known surveillance reporting biases in public repositories (Worldometer, USAFacts, Utah IBIS, Arizona DHS), the baseline parameters reflect a worst-case epidemiological setup:

1. **Infection and Recovery Adjustments:** Official active cases ($\approx 27,000$ in Arizona; $\approx 11,500$ in Utah) were scaled upward ($\approx 2.03\times$) to account for under-reporting and asymptomatic cases under a worst-case setup. Conversely, recovery rates (γ_j) are set as assumed baseline parameters to mitigate official tracking gaps and administrative auto-recovery reporting biases.

2. **Demographics and Mortality:** Birth rates (Λ_j) and natural mortality (μ_j) are converted from annual census statistics to daily per-capita rates normalized to a total meta-population of $N_1 + N_2 = 1,000$. Disease-induced mortality (δ_j) and demographic parameters (Λ_j, μ_j) are classified as Estimated parameters, accounting for state-specific reporting behaviors and conservative under-reporting adjustments.

3. **Inter-Regional Mobility Justification:** In the absence of direct empirical inter-state daily border-crossing logs during restriction periods, $m_{12} = 0.051$ day^{-1} and $m_{21} = 0.168$ day^{-1} are configured as assumed baseline parameters ($m_{21} > m_{12}$) grounded in regional socio-economic dynamics:

   - *Asymmetric Commuting Pressure ($m_{21} = 0.168$ day^{-1}):* Patch 2 (Utah) serves as a relatively smaller demographic and economic hub compared to Patch 1 (Arizona). Thus, a higher daily fraction (16.8%) of its population commutes to Patch 1 for work, trade, and essential services.
   - *Hub Retention ($m_{12} = 0.051$ day^{-1}):* Conversely, as Patch 1 (Arizona) acts as the primary regional economic center, a significantly lower fraction (5.1%) of its residents commutes outbound to Patch 2 daily.

   Symptomatic mobility rates are derived proportionally as $i_{jk} = \phi_j m_{jk} < m_{jk}$ ($\phi_j \in (0,1)$, $\phi_1 \approx 0.33, \phi_2 \approx 0.36$) to account for symptom-driven self-isolation.

The complete set of epidemiological parameters, parameter classifications, and data sources is summarized in Table 1. To properly capture memory and hereditary traits inherent to complex disease transmission, the fractional-order derivative is universally fixed at $\alpha = 0.8$, unless explicitly stated otherwise. For the susceptible, exposed, and recovered classes, we adopt the standard assumption of a baseline inter-regional mobility rate, setting $s_{jk} = e_{jk} = r_{jk} = m_{jk}$, where m_{jk} denotes the mobility rate from region j to region k. Biologically, individuals in the exposed class (E_j) are asymptomatic during the incubation period and unaware of their infectious status, rendering their commuting behavior indistinguishable from susceptible and recovered individuals. The system's state variables are normalized such that the total combined population across both regions equals 1,000 individuals, and are simulated from the following initial condition vectors:

$$S_1(0) = 0.1131, \quad E_1(0) = 0.10545, \quad I_1(0) = 0.01375, \quad R_1(0) = 0.2500, \tag{16}$$

$$S_2(0) = 0.1676, \quad E_2(0) = 0.01115, \quad I_2(0) = 0.01675, \quad R_2(0) = 0.3041. \tag{17}$$

The numerical integrations are carried out using a fractional-order PECE algorithm framework. To benchmark our findings, we categorize the global disease transmission dynamics under three primary regime archetypes determined by the transmission rates β_1 and β_2, which correspond to the following patch-specific (isolated) basic reproduction numbers:

1. **Disease extinction regime ($\mathscr{R}_0 < 1$):** $\beta_1 = 0.025$ and $\beta_2 = 0.002$, yielding $\mathscr{R}_0^{(1)} \approx 0.462521$ and $\mathscr{R}_0^{(2)} \approx 0.061498$.

Table 1: Parameter values, estimation classifications, and data sources for the representative two-patch SEIRS numerical experiment (Arizona as Patch 1, Utah as Patch 2, August 2020). The total meta-population is normalized to $N_1 + N_2 = 1{,}000$ ($N_1 = N_2 = 500$ per patch). All rate parameters are in units of day^{-1}.

Parameter	Value	Type / Source	Parameter	Value	Type / Source
Λ_1	0.013435 day^{-1}	Estimated[a,d]	Λ_2	0.01979 day^{-1}	Estimated[a,d]
θ_1	0.12147 day^{-1}	Estimated[d]	θ_2	0.11547 day^{-1}	Estimated[d]
μ_1	6.015×10^{-3} day^{-1}	Estimated[a,b]	μ_2	5.63×10^{-3} day^{-1}	Estimated[a,c]
δ_1	2.67742×10^{-3} day^{-1}	Estimated[d]	δ_2	3.87097×10^{-4} day^{-1}	Estimated[d]
γ_1	0.10634 day^{-1}	Assumed[e]	γ_2	0.102985 day^{-1}	Assumed[e]
m_{12}	0.051 day^{-1}	Assumed[f]	m_{21}	0.168 day^{-1}	Assumed[f]
i_{12}	0.017 day^{-1}	Derived[g]	i_{21}	0.061 day^{-1}	Derived[g]
ζ_1	0.29 day^{-1}	Assumed[h]	ζ_2	0.29 day^{-1}	Assumed[h]

Data Sources: [a]USAFacts; [b]Arizona DHS; [c]Utah IBIS; [d]Worldometer.

Parameter Notes:

[e]Assumed baseline recovery rates calibrated to mitigate official tracking gaps.

[f]Assumed baseline parameters modeling asymmetric inter-patch mobility.

[g]Reduced symptomatic mobility defined proportionally as $i_{jk} = \phi_j m_{jk}$ ($\phi_1 \approx 0.33, \phi_2 \approx 0.36$).

[h]Assumed baseline parameter modeling loss of temporary immunity ($\zeta_1 = \zeta_2 = 0.29$ day^{-1}) to demonstrate reinfection dynamics.

2. **Critical threshold tipping regime ($\mathscr{R}_0 \approx 1$):** $\beta_1 = 0.054052$ and $\beta_2 = 0.032523$, yielding $\mathscr{R}_0^{(1)} \approx 1.0000$ and $\mathscr{R}_0^{(2)} \approx 1.0000$.

3. **Epidemic persistent regime ($\mathscr{R}_0 > 1$):** $\beta_1 = 0.20097$ and $\beta_2 = 0.16516$, yielding $\mathscr{R}_0^{(1)} \approx 3.718116$ and $\mathscr{R}_0^{(2)} \approx 5.078465$.

When individual mobility between patches is absent ($m_{ij} = i_{ij} = 0$), the global reproduction number decouples cleanly into $\mathscr{R}_0 = \max\{\mathscr{R}_0^{(1)}, \mathscr{R}_0^{(2)}\}$. Depending on the relative weights of the patch-specific components, several independent sub-scenarios manifest for disease extinction ($\mathscr{R}_0^{(1)} \leq \mathscr{R}_0^{(2)} < 1$ or $\mathscr{R}_0^{(2)} \leq \mathscr{R}_0^{(1)} < 1$), critical transitions ($\mathscr{R}_0^{(1)} \leq \mathscr{R}_0^{(2)} \approx 1$ or $\mathscr{R}_0^{(2)} < \mathscr{R}_0^{(1)} \approx 1$), and epidemic expansion where one or both patches cross into persistence thresholds. The decoupled temporal trajectories of all epidemiological sub-classes under these parameter sets are illustrated in Fig. 2.

7.1 Impact of cross-border mobility on outbreak thresholds

To analyze the spatial interdependencies introduced by human commuting patterns, we track the long-term changes in the active classes-namely, the exposed (E_j) and infected (I_j) populations-at the terminal simulation horizon $T = 100$ days.

First, we fix the transmission capability of Region 1 at a low baseline value ($\beta_1 = 0.025$, rendering $\mathscr{R}_0^{(1)} < 1$) and sweep the transmission parameter of Region 2 across $\beta_2 \in [0.0, 4.0]$. Under the fully connected mobility framework, the terminal states of the active epidemic classes are plotted in Fig. 3. Theoretical computations indicate that for an isolated patch, a threshold boundary of $\mathscr{R}_0 = 1$ would require a high local transmission coefficient of $\beta_2 \approx 1.549006$. However, Fig. 3 reveals that as a consequence of coupling, as soon as β_2 surpasses the lower critical value of 0.03253, the populations of the active infectious classes escalate drastically in both regions simultaneously. This phenomenon is further intensified when the Reproduction value of Region 1 is raised to its own critical point ($\beta_1 = 0.054052$),

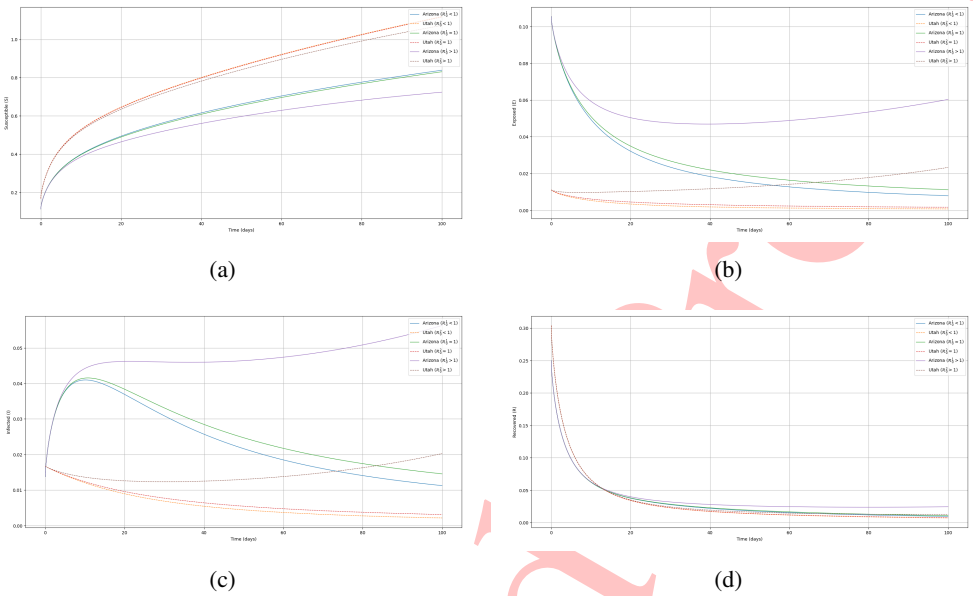

(a) (b)

(c) (d)

Figure 2: Variations of each class for $\alpha = 0.8$ when $m_{jk} = i_{jk} = 0$ for $\mathscr{R}_0^j < 1$, $\mathscr{R}_0^j = 1$ and $\mathscr{R}_0^j > 1$. (a) Susceptible populations, (b) Exposed populations, (c) Infected populations and (d) Recovered populations.

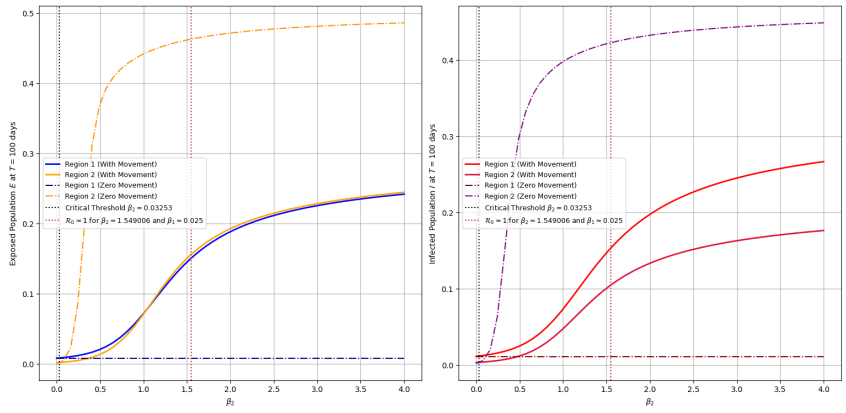

Figure 3: Parametric evaluation of the active epidemic classes at terminal time $T = 100$ days as a function of Region 2 transmission intensity β_2, evaluated under a low baseline transmission rate in Region 1 ($\beta_1 = 0.025$, $\mathscr{R}_0^{(1)} < 1$). The left panel shows the Exposed population E_j and the right panel shows the Infected population I_j across both coupled states.

as showcased in Fig. 4. Here, the cross-region spillover effectively compromises the safety margin of the entire meta-population long before the uncoupled threshold of $\beta_2 \approx 1.5641$ is mathematically achieved.

An analogous behavior is observed when evaluating the reverse configuration. Fixing the transmission capacity of Region 2 at a low baseline ($\beta_2 = 0.002$, rendering $\mathscr{R}_0^{(2)} < 1$) and sweeping Region 1 over $\beta_1 \in [0.0, 4.0]$ yields the parametric curves displayed in Fig. 5. While the individual uncoupled limit

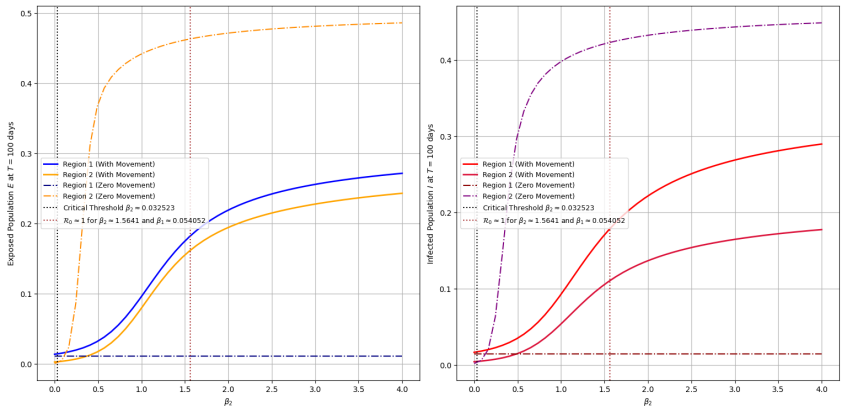

Figure 4: Parametric evaluation of the active epidemic classes at terminal time $T = 100$ days vs. β_2, where the baseline transmission index of Region 1 is elevated to its uncoupled critical threshold ($\beta_1 = 0.054052$, $\mathscr{R}_0^{(1)} \approx 1.0$). The trajectories demonstrate the long-term changes for the Exposed population E_j (left) and the Infected population I_j (right) due to coupling.

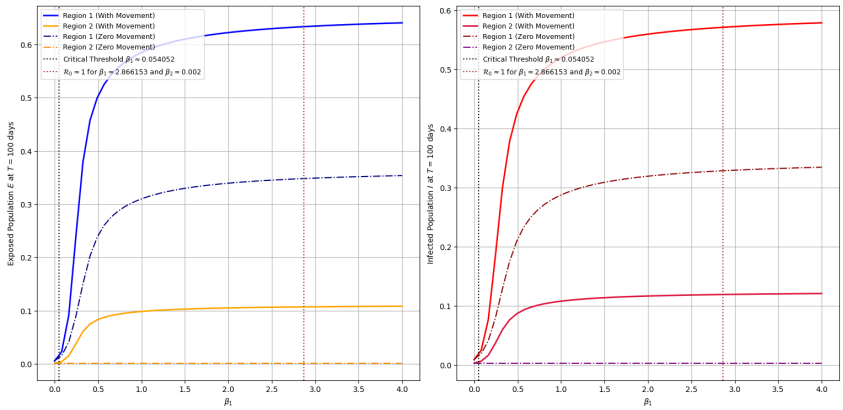

Figure 5: Influence of Region 1 transmission rate β_1 on active epidemic compartments at $T = 100$ days, assuming low baseline transmission in Region 2 ($\beta_2 = 0.002$, $\mathscr{R}_0^{(2)} < 1$). Exposed (E_j) and Infected (I_j) profiles are shown in the left and right panels, respectively, underscoring the outbreak acceleration induced by inter-regional commuting.

requires $\beta_1 \approx 2.866153$ to force $\mathscr{R}_0 = 1$, the introduction of cross-border commuting induces a sharp, significant rise in both exposed and infected cohorts on day 100 as soon as β_1 exceeds 0.054052. Elevating the baseline transmission index of Region 2 to $\beta_2 = 0.032523$ yields the trends in Fig. 6, driving an outbreak tipping point at an accelerated pace across both patches at approximately $\beta_1 \approx 2.8530$.

Collectively, Figs. 3 through 6 demonstrate that a rise in transmission intensity in one geographic zone inevitably degrades the epidemiological containment in the adjacent region due to human transport networks. However, by setting the system exactly at the coupled critical threshold ($\beta_1 = 0.054052$ and $\beta_2 = 0.065046$), the progression and stabilization of disease vectors over a 100-day window can be actively observed and monitored under real commuting behaviors (as shown in Fig. 7). Under identical parameter configurations, reducing the fractional-order from the classical integer case $\alpha = 1.0$ to

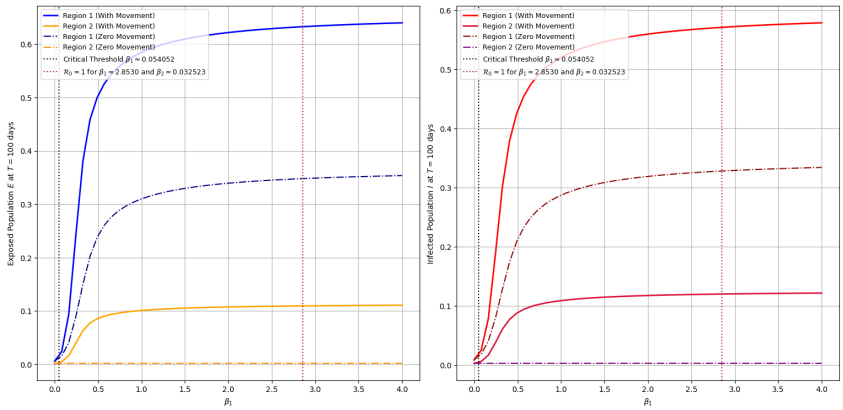

Figure 6: Response of active epidemic compartments at $T = 100$ days to variations in Region 1 transmission rate β_1, assuming Region 2 operates at its isolated threshold limit ($\beta_2 = 0.032523$, $\mathscr{R}_0^{(2)} \approx 1.0$). Left and right subplots display the system-wide dynamics of the Exposed (E_j) and Infected (I_j) classes, respectively, across the interconnected meta-population network.

fractional values $\alpha = 0.9, 0.8, 0.3$ systematically flattens and delays the epidemic trajectory in Region 1. Specifically, the peak infected population decreases from 0.04418 ($\alpha = 1.0$) to 0.04222 ($\alpha = 0.9$), 0.04054 ($\alpha = 0.8$), and 0.03537 ($\alpha = 0.3$), while the corresponding time-to-peak is delayed from $t = 7.30$ days to 8.40, 10.30, and 300.00 days, respectively. Furthermore, the cumulative recovered population at $T = 300$ drops from 0.00923 ($\alpha = 1.0$) to 0.00683 ($\alpha = 0.8$), whereas the strong memory tail at $\alpha = 0.3$ causes persistent long-term transients $R_1(300) = 0.11220$. In contrast, Region 2 remains consistently sub-threshold across all derivative orders, decaying monotonically from its initial state $I_2(0.0) = 0.01675$. This shift highlights how fractional-order memory inherently dampens transmission intensity and slows down epidemic progression across interconnected regions.

7.2 Evaluation of optimal public health controls

To mitigate the rapid spatial spread of infection highlighted in our mobility analysis, it becomes necessary to evaluate intervention strategies, such as targeted public-health directives and regional vaccination policies. Accordingly, Fig. 8 (a),(d),(g) and (j) presents the 100-day dynamic profiles of both states under conditions of asymmetric mobility connecting actively controlled and uncontrolled environments. These optimal control simulations are evaluated under severe epidemic conditions ($\beta_1 = 0.20097$ and $\beta_2 = 0.16516$), utilizing the same initial conditions outlined above. The quadratic cost functional is computed assuming symmetric optimization weights $A_j = 20$ and $B_j = 1$, with the maximum allowable intervention intensity upper-bounded at $u_{j,\max} = 1$ for both patches ($j = 1, 2$). The corresponding controller behavior over this time interval is illustrated in Fig. 9 (a).

On the other hand, Fig. 8 (b),(e),(h) and (k) shows the system dynamics when the initial condition is the endemic equilibrium. Without control, the system remains at the endemic equilibrium throughout the simulation. When the optimal controller is applied, the expected convergence is observed while the control input is maintained at its maximum admissible value. These dynamics are presented over a 100-day period, and the corresponding control inputs are shown in Fig. 9 (b).

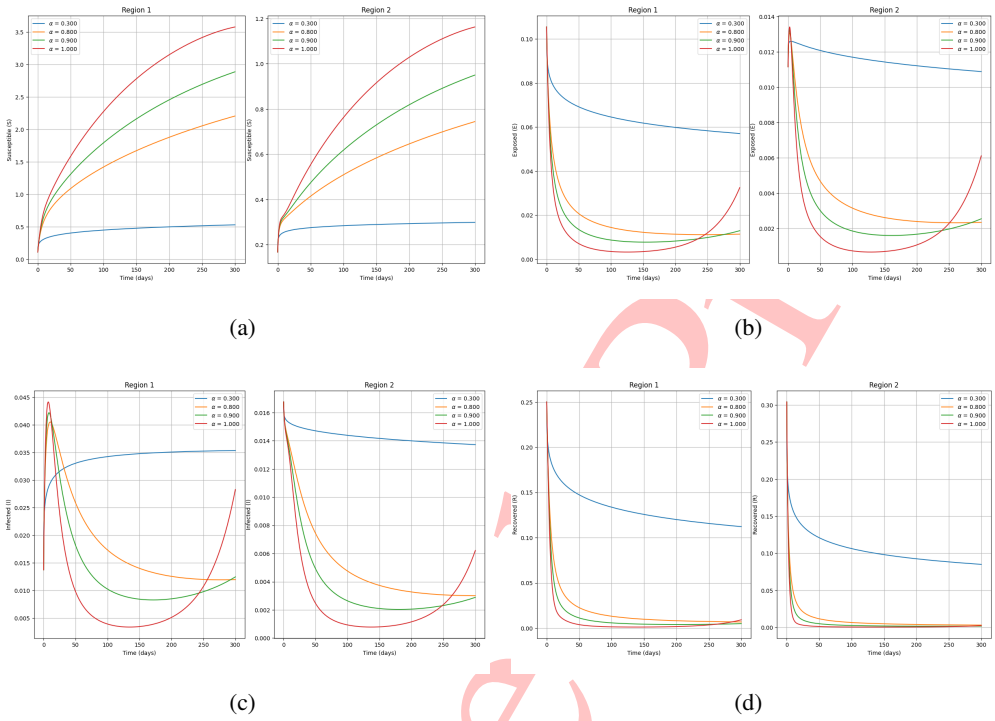

Figure 7: Variations of each class for $\alpha = 0.3, 0.8, 0.9$ and 1.0 when $m_{jk}, i_{jk} \neq 0$ for $\mathscr{R}_0^j = 1$. (a) Susceptible populations, (b) Exposed populations, (c) Infected populations and (d) Recovered populations.

To assess the sensitivity of the optimal solution to the weighting coefficients, the ratio A_j/B_j was reduced to 0.05, while all other parameters were kept unchanged. The corresponding epidemic trajectories and optimal control profiles are shown in Figs. 8 (c), (f), (i) and (l), and Fig. 9 (c), respectively. The resulting optimal controls remain below 0.008 and 0.001 for $u_1^*(t)$ and $u_2^*(t)$, respectively, indicating that smaller values of A_j/B_j lead to less aggressive intervention policies due to the increased relative cost of control.

From an economic perspective, the weighting coefficients reflect the trade-off between the epidemiological benefits of reducing infections and the costs associated with implementing control measures. Consequently, their selection provides public health decision-makers with a quantitative mechanism for designing intervention strategies that are consistent with available resources and the desired level of epidemic mitigation. The resulting curves highlight the efficiency of the applied fractional controller in rapidly suppressing active infectious vectors across both coupled territories despite high core transmission rates. For further details, see Appendix.

8 Conclusion

This paper investigated a multi-region fractional-order SEIRS epidemic model incorporating inter-regional mobility, spatial coupling, and reinfection effects. The mathematical framework was formulated utilizing Caputo fractional derivatives to systematically capture memory-dependent transmission dynamics and

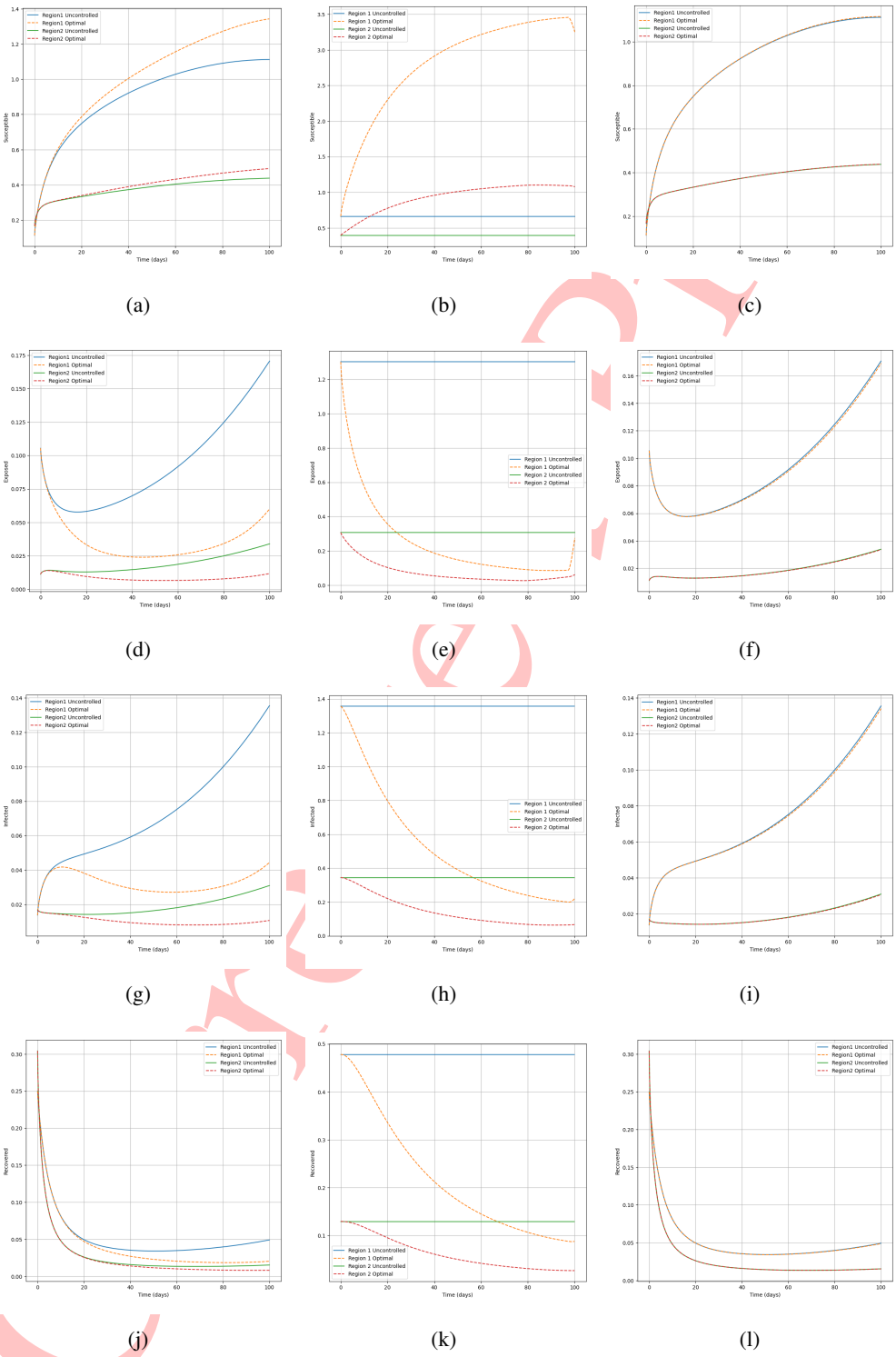

Figure 8: Comparison between the uncontrolled system and the controlled system with $\alpha = 0.8$. (a–c) Susceptible populations , (d–f) Exposed populations, (g–i) Infected populations and (j–l) Recovered populations.

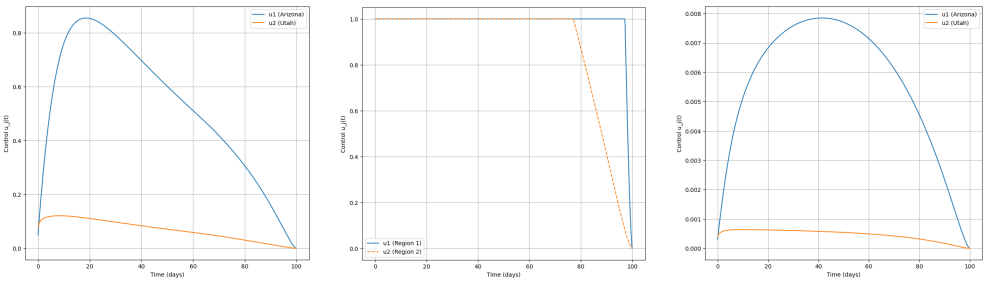

(a) (b) (c)

Figure 9: Optimal control inputs $u_1(t)$ and $u_2(t)$ over the interval $[0, 100]$.

hereditary traits across patch boundaries. In particular, it was proven that the disease-free equilibrium is globally asymptotically stable when the global basic reproduction number satisfies $\mathscr{R}_0 < 1$, whereas a unique endemic equilibrium exists and exhibits global asymptotic stability when $\mathscr{R}_0 > 1$. Crucially, the global stability of the endemic equilibrium is proven under a specific proportionality assumption on mobility rates, which may not generally hold for empirical movement data.

Complementing the analytical derivations, extensive numerical simulations were executed using PECE algorithm parameterized with empirical COVID-19 data from Arizona and Utah. The numerical outcomes provided critical insights into the practical implications of spatial connectivity within a meta-population framework. Notably, parametric sensitivity sweeps of the transmission rates (β_1, β_2) revealed that cross-border commuting patterns profoundly deform individual patch thresholds. Even when a focal region maintains a local reproduction number well below unity ($\mathscr{R}_0^{(j)} < 1$), intensive mobility coupling with an adjacent, high-transmission patch can prematurely compromise its epidemiological containment, sparking synchronized outbreaks across both territories long before isolated threshold limits are reached. Furthermore, the implementation of a fractional optimal control framework demonstrated that coordinated public health directives and vaccination policies can successfully suppress infectious trajectories even under severe epidemic persistence regimes, highlighting the utility of fractional-order control loops in real-world multi-patch interventions. Although the numerical examples are presented for a two-region network for clarity, the proposed multi-region model and the associated optimality conditions are formulated for an arbitrary number of interconnected regions. Extending the framework to larger networks does not alter the underlying theoretical results; however, it increases the dimension of the coupled state adjoint system and, consequently, the computational effort required for its numerical solution.

Future research will focus on extending the proposed framework to multi-patch epidemic models governed by time-varying reproduction numbers and non-autonomous transmission parameters. Such extensions will offer a more realistic and granular description of seasonal temporal variations in disease transmission and evolving public health policies. Another important direction for future work is relaxing the proportionality condition on mobility rates to establish the global stability of the endemic equilibrium under general movement dynamics. Additionally, developing scalable and computationally efficient numerical algorithms for solving the fractional optimal control system in large-scale multi-region networks remains a priority. Further extensions include the incorporation of an unidentified infected individual class, the investigation of nonlinear alternative incidence functions, the integration of higher-

dimensional network data representing multi-state transport matrices, and the development of stochastic fractional-order epidemic models to formally account for environmental, behavioral, and demographic uncertainties.

Appendix

In this appendix, we present details of the numerical framework used to solve the optimal control problem governed by Caputo fractional differential equations. Both the state system (in t) and the time-reversed co-state system (in $\tau = T - t$) are discretized on a uniform temporal mesh $t_n = n\Delta t$ $(n = 0, 1, \ldots, N)$ with step size $\Delta t = T/N$. We employ the Diethelm Predictor-Evaluate-Corrector-Evaluate (PECE) fractional Adams-Bashforth-Moulton method. For the fractional state system ${}_0^C D_t^\alpha \mathbf{y}(t) = \mathbf{f}_{\text{state}}(\mathbf{y}(t), \mathbf{u}(t))$ and co-state system ${}_0^C D_\tau^\alpha \tilde{\boldsymbol{\lambda}}(\tau) = \mathbf{g}_{\text{costate}}(\tilde{\boldsymbol{\lambda}}(\tau), \mathbf{y}_{\text{rev}}(\tau), \mathbf{u}_{\text{rev}}(\tau))$, the scheme evaluates with initial condition $\mathbf{y}(0) = \mathbf{y}_0$:

1. **Predictor Step:**

$$\mathbf{y}_{n+1}^P = \mathbf{y}_0 + \frac{(\Delta t)^\alpha}{\Gamma(\alpha+1)} \sum_{j=0}^{n} b_{j,n+1} \mathbf{f}_{\text{state}}(t_j, \mathbf{y}_j, \mathbf{u}_j), \tag{18}$$

   where the weight coefficients $b_{j,n+1}$ are given by:

$$b_{j,n+1} = (n+1-j)^\alpha - (n-j)^\alpha.$$

2. **Corrector Step:**

$$\mathbf{y}_{n+1} = \mathbf{y}_0 + \frac{(\Delta t)^\alpha}{\Gamma(\alpha+2)} \left[\mathbf{f}_{\text{state}}(t_{n+1}, \mathbf{y}_{n+1}^P, \mathbf{u}_{n+1}) + \sum_{j=0}^{n} a_{j,n+1} \mathbf{f}_{\text{state}}(t_j, \mathbf{y}_j, \mathbf{u}_j) \right], \tag{19}$$

   where the weight coefficients $a_{j,n+1}$ are defined as:

$$a_{j,n+1} = \begin{cases} n^{\alpha+1} - (n-\alpha)(n+1)^\alpha, & j = 0, \\ (n-j+2)^{\alpha+1} + (n-j)^{\alpha+1} - 2(n-j+1)^{\alpha+1}, & 1 \le j \le n. \end{cases}$$

The complete numerical implementation is outlined in Algorithm 1. In all executed numerical scenarios, the algorithm consistently satisfies the relative tolerance criterion within 7 to 12 iterations—well below the prescribed upper limit.

Acknowledgements

We thank the anonymous reviewers for thoughtful comments and constructive suggestions that strengthened the manuscript.

Declarations

Ethical approval: Not applicable.

Algorithm 1: Fractional PECE Forward-Backward Sweep Method

Require: Initial state $\mathbf{y}_0 = [S_1(0), S_2(0), E_1(0), E_2(0), I_1(0), I_2(0), R_1(0), R_2(0)]^T$, final time $T = 100$, step size $\Delta t = 0.1$, fractional-order $\alpha = 0.8$, tolerance tol $= 10^{-4}$, maximum iterations $k_{\max} = 30$, upper bound $u_{\max} = 1.0$, weight parameters $A_j = 20.0, B_j = 1.0$ for $j \in \{1,2\}$.

Ensure: Optimal states $\mathbf{y}^*(t)$, co-states $\boldsymbol{\lambda}^*(t)$, and controls $\mathbf{u}^*(t)$.

Initialize control array $\mathbf{u}^{(0)}(t_n) = [0,0]^T$ for all $n = 0, 1, \ldots, N$.
Set iteration count $k = 1$, converged = False.
repeat
  % Step 1: Forward State Solution
  Solve ${}_0^C D_t^\alpha \mathbf{y}^{(k)}(t) = \mathbf{f}_{\text{state}}(\mathbf{y}^{(k)}(t), \mathbf{u}^{(k-1)}(t))$ forward in $t \in [0,T]$ with initial condition $\mathbf{y}^{(k)}(0) = \mathbf{y}_0$ using the state system defined in Eq. (7) via the Diethelm PECE method.
  % Step 2: Time-Reversal and Backward Co-State Solution
  Construct time-reversed state and control arrays for $n = 0, 1, \ldots, N$:
    $\mathbf{y}_{\text{rev}}(t_n) = \mathbf{y}^{(k)}(T - t_n)$ and $\mathbf{u}_{\text{rev}}(t_n) = \mathbf{u}^{(k-1)}(T - t_n)$.
  Solve ${}_0^C D_\tau^\alpha \tilde{\boldsymbol{\lambda}}^{(k)}(\tau) = \mathbf{g}_{\text{costate}}(\tilde{\boldsymbol{\lambda}}^{(k)}(\tau), \mathbf{y}_{\text{rev}}(\tau), \mathbf{u}_{\text{rev}}(\tau))$ forward in $\tau \in [0,T]$ using the adjoint system defined in Eq. (14) with initial condition $\tilde{\boldsymbol{\lambda}}^{(k)}(0) = \mathbf{0}$ via the Diethelm PECE method.
  Restore co-states in original time domain: $\boldsymbol{\lambda}^{(k)}(t_n) = \tilde{\boldsymbol{\lambda}}^{(k)}(T - t_n)$.
  % Step 3: Control Characterization and Bounded Update
  for each time grid point $n = 0, 1, \ldots, N$ and patch $j \in \{1,2\}$ **do**
    $u_j^{\text{raw}}(t_n) = \dfrac{\beta_j S_j^{(k)}(t_n) I_j^{(k)}(t_n) \left(\lambda_{2,j}^{(k)}(t_n) - \lambda_{1,j}^{(k)}(t_n)\right)}{B_j}$
    $u_j^{(k)}(t_n) = \min\left(u_{\max}, \max\left(0, u_j^{\text{raw}}(t_n)\right)\right)$
  end for
  % Step 4: Relative Convergence Evaluation
  Compute relative Euclidean norm change:
    $E^{(k)} = \frac{\|\mathbf{u}^{(k)} - \mathbf{u}^{(k-1)}\|_2}{\|\mathbf{u}^{(k-1)}\|_2 + 10^{-8}}$ where $\|\mathbf{u}\|_2 = \sqrt{\sum_{n=0}^{N} \sum_{j=1}^{2} |u_j(t_n)|^2}$
  if $E^{(k)} <$ tol **then**
    converged = True
  else
    $k = k + 1$
  end if
until converged = True **or** $k > k_{\max}$

Competing interests: The authors declare that they have no competing interests.

Authors' contributions: All authors contributed equally to the manuscript, read, and approved the final version.

Funding: Not applicable.

Availability of data and materials: Not applicable.

References

[1] A. Abd-Elmonem, R. Banerjee, S. Ahmad, W. Jamshed, K.S. Nisar, M.R. Eid, R.W. Ibrahim, S.M. El Din, *A comprehensive review on fractional-order optimal control problem and its solution*, Open Math. **21** (2023) 20230105.

[2] R. Agarwal, S. Hristova, D. O'Regan, *A survey of Lyapunov functions, stability and impulsive Caputo fractional differential equations*, Fract. Calc. Appl. Anal. **19** (2016) 290–318.

[3] O.P. Agrawal, *A general formulation and solution scheme for fractional optimal control problems*, Nonlinear Dynam. **38** (2004) 323–337.

[4] A. Berman, R.J. Plemmons, *Nonnegative Matrices in the Mathematical Sciences*, SIAM, 1994.

[5] N.P. Bhatia, G.P. Szegö, *Dynamical Systems: Stability Theory and Applications*, Springer, 2006.

[6] F. Brauer, C. Castillo-Chavez, Z. Feng, *Epidemiological models incorporating mobility, behavior, and time scales*, in: Mathematical Models in Epidemiology, Texts in Applied Mathematics, vol. 69, Springer, New York, NY, 2019, 477–504.

[7] L. Cesari, *Problems of optimization: A general view*, in: Optimization Theory and Applications: Problems with Ordinary Differential Equations, Springer, 1983, pp. 1–23.

[8] E. Deutsch, *The spectral abscissa of partitioned matrices*, J. Math. Anal. Appl. **50** (1975) 66–73.

[9] B. Diallo, M. Dasumani, J.A. Okelo, S. Osman, O. Sow, N.S. Aguegboh, W. Okongo, *Fractional optimal control problem modeling bovine tuberculosis and rabies co-infection*, Results Control Optim. **18** (2025) 100523.

[10] K. Diethelm, N.J. Ford, A.D. Freed, *A predictor-corrector approach for the numerical solution of fractional differential equations*, Nonlinear Dynam. **29** (2002) 3–22.

[11] F. El Kihal, M. Rachik, O. Zakary, I. Elmouki, *A multi-regions SEIRS discrete epidemic model with a travel-blocking vicinity optimal control approach on cells*, Int. J. Adv. Appl. Math. Mech. **4** (2017) 60–71.

[12] I. Elmouki, L. Zhong, A. Jraifi, A. Darouichi, *Optimal control: application and applicability in times of pandemics*, in: Integrated Science of Global Epidemics, Springer International Publishing, Cham, 2023, pp. 191–210.

[13] A.F. Filippov, *On certain questions in the theory of optimal control*, J. Soc. Indust. Appl. Math. Ser. A Control **1** (1962) 76–84.

[14] J. Huo, H. Zhao, L. Zhu, *The effect of vaccines on backward bifurcation in a fractional order HIV model*, Nonlinear Anal. Real World Appl. **26** (2015) 289–305.

[15] M. Kretzschmar, *Disease modeling for public health: added value, challenges, and institutional constraints*, J. Public Health Policy **41** (2020) 39–51.

[16] M.Y. Li, J.R. Graef, L. Wang, J. Karsai, *Global dynamics of a SEIR model with varying total population size*, Math. Biosci. **160** (1999) 191–213.

[17] M.Y. Li, Z. Shuai, *Global-stability problem for coupled systems of differential equations on networks*, J. Differ. Equ. **248** (2010) 1–20.

[18] M.Y. Li, *An Introduction to Mathematical Modeling of Infectious Diseases*, Springer, 2018.

[19] B. Lieberthal, A. Soliman, S. Wang, S. De Urioste-Stone, A.M. Gardner, *Epidemic spread on patch networks with community structure*, Math. Biosci. **359** (2023) 108996.

[20] W. Lin, *Global existence theory and chaos control of fractional differential equations*, J. Math. Anal. Appl. **332** (2007) 709–726.

[21] A.B. Malinowska, T. Odzijewicz, D.F.M. Torres, *Advanced Methods in the Fractional Calculus of Variations*, Springer, 2015.

[22] A.S. Mata, S.M. Dourado, *Mathematical modeling applied to epidemics: an overview*, São Paulo J. Math. Sci. **15(2)** (2021) 1025–1044.

[23] D. Matignon, *Stability results for fractional differential equations with applications to control processing*, in: IEEE CESA Multiconf., vol. 2, Lille, France, 1996, 963–968.

[24] O. Saucedo, J.H. Tien, *Host movement, transmission hot spots, and vector-borne disease dynamics on spatial networks*, Infect. Dis. Model. **7** (2022) 742–760.

[25] H.L. Smith, P. Waltman, *The Theory of the Chemostat: Dynamics of Microbial Competition*, Cambridge University Press, Cambridge, 1995.

[26] W.M. Sweileh, *Global research activity on mathematical modeling of transmission and control of 23 selected infectious disease outbreak*, Glob. Health **18** (2022) 1–14.

[27] P. Van den Driessche, J. Watmough, *Reproduction numbers and sub-threshold endemic equilibria for compartmental models of disease transmission*, Math. Biosci. **180** (2002) 29–48.

[28] C. Vargas-De-León, *Volterra-type Lyapunov functions for fractional-order epidemic systems*, Commun. Nonlinear Sci. Numer. Simul. **24** (2015) 75–85.

[29] C. Wu, *Comparison principles for systems of Caputo fractional order ordinary differential equations*, Chaos Solit. Fractals **170** (2023) 113377.

[30] X.-Q. Zhao, *Dynamical Systems in Population Biology*, 2nd ed., Springer, Cham, 2017.